Journal of Materials Chemistry A

ROYAL SOCIETY OF CHEMISTRY

PAPER

View Article Online
View Journal | View Issue

Cite this: J. Mater. Chem. A, 2023, 11, 7662

Interfacial charge transfer weakens hydrogen bonds between water molecules to accelerate solar water evaporation†

Liru Wang,[ab] Jinguo Lin,[c] Yuanyuan Li,[a] Yanan Yang,[ab] Xiaoting Liu,[a] Zhe Wang,[a] Feng Liu, *[c] Xiaotong Sun,[a] Tian Yang,[ab] Nan Chen *[ab] and Liangti Qu [d]

The evaporation of water requires considerable energy as it must break the hydrogen bonds that account for 5/6 of the total intermolecular forces of water in addition to breaking the intermolecular forces. The same is true for solar interfacial water evaporation to produce pure water. The problem of how to weaken the hydrogen bonds between liquid water molecules in a solar absorber below the boiling point of water to increase the evaporation rate has not been focused upon. We designed a reduced graphene oxide (rGO)-based foam (rGOFpl foam) with a surface rich in highly polar units as a solar absorber. Theoretical simulations confirm that the charge transfer at the solid–liquid interface brought by highly polar units such as MgF_2 affects the charge distribution of adjacent water molecules, forming more interstitial water layers with weak intermolecular hydrogen bonds and easy evaporation. rGOFpl foam has a water vapor production rate of 1.83 kg m^{-2} h^{-1} under 1 kW m^{-2} solar radiation, which is 1.87 times higher than that of the rGO foam and much higher than some previously reported ones for certain conventional rGO-based solar absorbers. This study provides an important theoretical basis for the design of future solar thermal absorbers and paves the way for the practical application of cost-effective solar interfacial water evaporation technology.

Received 20th December 2022
Accepted 2nd March 2023

DOI: 10.1039/d2ta09891a

rsc.li/materials-a

Introduction

Solar-driven interfacial water evaporation involves the generation of water vapor by breaking the hydrogen bonds between water molecules at a temperature below the boiling point of water. In the past, scientists have mainly focused on designing novel structures and selecting materials with better photothermal properties to enhance the water evaporation rate.[1–13] For example, Lu *et al.* designed a hydrophobic nano-constrained water molecular channel (NCWMC), which limits the volume of water clusters transported in the channel, achieving a record steam generation rate of 1.25 kg m^{-2} h^{-1} under 0.5 sun radiation.[14] Li *et al.* prepared a polymer "ET" with ultralow band gap by introducing a strong receptor unit with vertical π expansion, achieving ultrafast internal conversion process (1.49 ps), showing excellent photothermal conversion efficiency of 50.3% under 1064 nm irradiation, and achieving effective NIR light utilization.[15]

However, the fundamental pathway of promoting the rate of water evaporation under photothermal conditions by weakening the hydrogen bonds between water molecules to reduce the evaporation enthalpy has not been focused upon. Hydrogen bonding is a type of intermolecular force, a force between permanent dipoles, which occurs between a hydrogen atom that is already covalently bonded to other atoms and another atom that is more electronegative (X–H···Y).[16] In the case of water, for example, liquid water must break intermolecular hydrogen bonds in addition to breaking intermolecular forces when it is vaporized. Calculations show that the bonding energy of hydrogen bonds must account for 5/6 of the total intermolecular forces between liquid water molecules, thus causing water to have a much higher boiling point than other common liquids. Water in interfacial solar evaporation materials generally exists in three forms, namely, free water (FW), intermediate water (IW), and bound water (BW).[17–20] In addition to FW, which has no interaction force with the hydrophilic evaporation material, both IW and BW will interact with the evaporation material through hydrogen bonding. The difference is that FW has a weaker hydrogen bond with the photothermal material

[a]Key Laboratory of Cluster Science, Ministry of Education of China, Key Laboratory of Photoelectronic/Electrophotonic Conversion Materials, School of Chemistry and Chemical Engineering, Beijing Institute of Technology, Beijing 100081, P. R. China. E-mail: gabechain@bit.edu.cn

[b]Yangtze Delta Region Academy of Beijing Institute of Technology, Jiaxing, 314019, China

[c]State Key Laboratory of Nonlinear Mechanics Institute of Mechanics, Chinese Academy of Sciences, Beijing 100083, P. R. China. E-mail: liufeng@imech.ac.cn

[d]Key Laboratory of Organic Optoelectronics & Molecular Engineering, Ministry of Education, Department of Chemistry, Tsinghua University, Beijing 100084, China

† Electronic supplementary information (ESI) available. See DOI: https://doi.org/10.1039/d2ta09891a

compared to the BW. The reason why IW with weaker hydrogen bonds is the bulk of the water produced by interfacial solar evaporation is that they tend to escape below the boiling point.[21–24]

Highly polar surface rGOFpl foam was designed as an interfacial solar evaporation absorber by loading fluorphlogopite ($KMg_3(AlSi_3O_{10})F_2$) nanosheets (Fpl nanosheets), which contains numerous highly electronegative F and O atoms onto three-dimensional (3D)-reduced graphene oxide (rGO). rGOFpl foam exhibited an 86.7% increase in the water evaporation rate over conventional rGO foam, reaching up to 1.83 kg m^{-2} h^{-1}, which is higher than the most common rGO-based solar absorbers in terms of the actual evaporation utilization area. The highly polar surface of rGOFpl foam causes a redistribution of the charge of water molecules in the adjacent BW layer, which in turn affects the change un the intermolecular hydrogen bonding of the adjacent IW. First-principles calculations (FP calculations) and molecular dynamics simulations (MD simulations) explain the mechanism by which the uniformly dispersed strongly polar Fpl nanosheets on the rGO surface affect the charge distribution of water molecules in the adjacent BW layer. The weakening effect of hydrogen bonding in the IW layer when the BW layer is disturbed by polarity greatly accelerates the evaporation rate of water in the rGOFpl foam.

Experimental

Materials

Natural graphite (325 mesh, Tianjin Graphite Company) and fluorophlogopite (Fpl) flakes (about 5 mesh, Anhui Hengyue Mineral Products Processing Factory) were purchased. Other conventional chemicals and reagents are purchased from Xilong Chemical Co., Ltd.

Preparation of rGO and rGOFpl foams

Fpl nanosheets were obtained by ball milling thin flakes of Fpl for 48 h. GO solution was prepared from natural graphite powder by a modified Hummers' method.[25] Different masses of Fpl were mixed with GO solution (5 mg mL^{-1}) and ultrasonically dispersed, then mixed with ethanol in a 30 : 1 volume ratio and poured into a mold to be freeze-dried to obtain GOFpl foams. The rGOFpl foams were obtained by reducing GOFpl foams with hydrazine vapor in an oil bath at 80 °C. The samples were cut by a laser to obtain the desired size for later testing.

Solar steam generation experiments

The foam (1.0 × 1.0 cm) was placed on top of the water-filled container and isolated with polystyrene foam as an insulating layer, using absorbent swabs for the most water delivery medium. The whole device was placed under solar simulation with different optical concentrations. Solar steam generation rate was measured for 60 min at steady state. Weight change was measured by an electronic balance and the surface temperature was recorded by an infrared camera.

Determination of equivalent enthalpy of evaporation and energy conversion efficiency

The equivalent enthalpy of evaporation was determined by the dark evaporation method. The mass change of pure water, water in rGO, and rGOFpl foam at the same time were recorded under complete darkness, and the equivalent enthalpy of evaporation of water in the foam was calculated using eqn (1) as follows.

$$\Delta H_{vap} m_0 = \Delta H_{equ} m_g \quad (1)$$

where ΔH_{vap} and m_0 are the enthalpy of evaporation and mass change of pure water, respectively, and m_g is the mass change of the foam. Based on this, energy conversion efficiency (η) is calculated using eqn (2).[26]

$$\eta = m h_v / C_{opt} P_0 \quad (2)$$

where m is the mass flux, h_v is the evaporation enthalpy of water in the rGOFpl foam, P_0 is the solar irradiation of 1 sun (1 kW m^{-2}), and C_{opt} is the optical concentration on the absorber surface.

Simulated solar desalination and wastewater treatment performance tests

To evaluate the water purification performance of rGOFpl foam, five foams (1 × 1 cm) were used to purify the sea water from the China's Yellow Sea, and five simulated wastewaters (metronidazole, atenolol, ciprofloxacin, ibuprofen, Rhodamine B) under simulated solar irradiation. The concentrations of major metal ions and drugs in the original solution, condensate, and collected water were determined by an inductively coupled plasma atomic emission instrument, UV vis spectrophotometry, and standard absorption curve method.

Characterization

X-ray diffraction (XRD) patterns were recorded on a Netherlands 1710 diffractometer with a Cu Kα radiation source $\left(1\frac{1}{4}\ 1.54\ \text{Å}\right)$. The morphology of the samples and the energy dispersive X-ray spectra (EDX) were obtained by scanning electron microscopy (SEM) (Zeiss SUPRA TM 55 SAPPHIRE, Germany). The atomic ratios of rGO and rGOFpl foam were characterized using X-ray photoelectron spectroscopy (XPS). The XPS results were obtained with an ESCALab220i-XL electron spectrometer from VG Scientific using 300 W Al Kα radiation. Mechanical compression test was carried out on a SHIMADZU AGS-X. The reflection (R) and transmission (T) spectra of rGO and rGOFpl foams and wastewater purification curves were measured on a Shimadzu UV vis spectrophotometer (UV 3600) with an integrating sphere diffuse reflectance. Absorptivity (A) was calculated by the formula: $A = 1 - R - T$. The Fourier transform infrared reflection (FTIR) spectra of rGO and rGOFpl foam were obtained by a Fourier transform infrared spectrometer (IS5) in the range of 400–4000 cm^{-1}. *In situ* Diffuse Reflectance Infrared Fourier Transform (DRIFT) spectra were obtained in the range of 500–4000 cm^{-1} by a BRUKER TENSOR

II. The Raman spectra were obtained using an RM 2000 Microscopic Confocal Raman Spectrometer (Renishaw PLC, England) with a 532 nm laser. Foam evaporation enthalpy was measured by differential thermal analysis (DSC) (TA Q2000, America). The temperature was measured by an IR camera (Fluke TiX640). The weight change of water was measured by an electronic mass balance with an accuracy of 0.0001 g. The steam generation experiments were performed in the laboratory using a solar simulator (MC-X301B). The ion concentration of the collected water was measured by an inductively coupled plasma emission spectrometer (ICPE-9820, Shimadzu).

Results and discussion

Fig. 1a is a schematic diagram of the preparation process and evaporation system composition of rGOFpl foam. The dispersion containing Fpl nanosheets (Fig. 1b) with GO was freeze-dried to obtain GOFpl foam. Shape-regular rGOFpl foam was obtained by allowing GOFpl foam to be reduced by hydrazine vapor and then laser cut (see Fig. S1 and S2†) for detail. rGOFpl foams with different mass ratios (Fpl : GO) including 1 : 1, 1 : 2, 1 : 3, and 1 : 5 were prepared and named rGOFpl-1, rGOFpl-2, rGOFpl-3, and rGOFpl-5, respectively; rGO was also prepared. The optimization experiments in Fig. 3b shows that rGOFpl-3 has the best performance for solar water evaporation, and all subsequent tests were conducted with rGOFpl-3, abbreviated as rGOFpl.

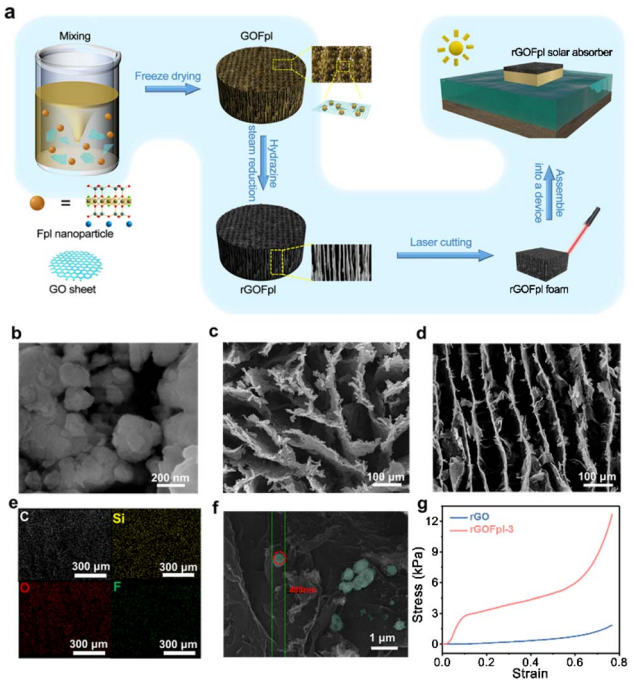

Fig. 1 (a) Schematic illustration for the fabrication of rGOFpl foam. SEM image of (b) Fpl nanosheets. SEM images of the rGOFpl-3 foam in (c) top view and (d) side view along the vertical channel. (e) EDX elemental mapping analysis of the rGOFpl-3 foam. (f) Fpl nanosheets attached to graphene sheets in rGOFpl-3 foam. (g) Compressive stress–strain curves of rGO and rGOFpl-3 foam under compressive strain (axial).

The surface of the rGOFpl foam consists of many folded graphene nanosheets in a typical 3D porous network structure, and all have high porosity (>99%), as shown in Fig. S3,† 1c, Table S1, and Note S1,† which will effectively increase the absorption surface area of sunlight and produce higher light absorption efficiency. The ethanol used for freeze conditioning rGOFpl foam morphology allows the graphene nanosheets to form regular vertical channels up to tens of microns in diameter, as shown in Fig. 1d, which is very helpful for rapid water transport from the bottom to the upper evaporation interface. The EDX spectra of Fpl shows that the main elements in Fpl nanosheets are O, Si, Mg, and F, which are also uniformly dispersed in the rGOFpl foam (EDX elemental mapping analysis in Fig. 1e and Table S2†). Due to the large surface energy and surface polarity, many rigid Fpl nanosheets with a diameter of about 500 nm are firmly attached to the graphene sheets, as shown in Fig. 1f. The presence of Fpl nanosheets enhances the strength of graphene backbone, resulting in higher mechanical stability of the rGOFpl foam, as shown in Fig. 1g. It is also possible to demonstrate that the Fpl nanosheets have been doped into rGO by observing the characteristic peak at 26° in the X-ray diffraction data (XRD) pattern in Fig. 2a. With reference to the data on the elemental content in EDX (Tables S3 and S4†), the characteristic peak of Si–O–Si was also observed at 531.8 eV in the X-ray photoelectron (XPS) spectra of rGOFpl, as shown in Fig. 2b.

Due to the sensitivity of hydrogen bonding to the chemical environment, the change in its state in water can be obtained by analyzing the chemical shift in the stretching vibrational peaks of –OH. The FTIR spectra in Fig. 2c showed that the –OH peaks of rGOFpl with different contents of Fpl are redshifted compared to the characteristic peak of rGO at 3288 cm^{-1}, and this redshift can be seen more clearly in the magnified view of selected regions, as shown in Fig. S4 and Note S2.† Among

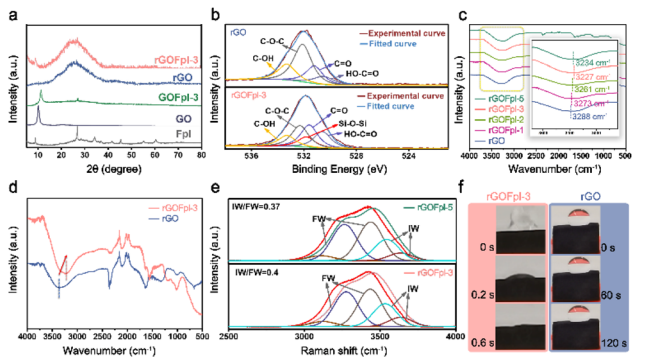

Fig. 2 (a) XRD characterization of Fpl, GO, GOFpl-3, rGO, and rGOFpl-3. (b) XPS characterization of rGO and rGOFpl-3. (c) FTIR spectra of rGO and rGOFpl with different mass ratios (Fpl : GO) of 1 : 1, 1 : 2, 1 : 3, and 1 : 5. The inset figure is the larger view of peak of –OH in the water molecules. (d) The FTIR spectra of wet rGO and rGOFpl-3 without sunlight exposure. The blue line indicates the –OH peak of rGO and the red line indicates the –OH peak of rGOFpl-3. (e) Raman spectra with fitting curves showing the ratio of IW to FW in the rGOFpl-5 (the top) and rGOFpl-3 (the bottom). (f) Wetting of rGO and rGOFpl-3 at different times.

them, rGOFpl-3 (3227 cm^{-1}) has the largest redshift, indicating that the polar surface of the Fpl nanosheets forms the most hydrogen bonds with water molecules. The apparent redshifts of the –OH absorption peaks of rGO and rGOFpl-3 at 3376 cm^{-1} and 3211 cm^{-1}, respectively, when they are not exposed to sunlight in Fig. 2d proves that sunlight exposure is not related to the hydrogen bonds formed between the Fpl nanosheets and water molecules. The presence of Fpl allows more IW molecules with weaker intermolecular hydrogen bonds to escape more easily from the evaporation interface. *In situ* DRIFT spectra show that there is only one large and broad water –OH peak in rGO, which is the FW –OH peak. The area of the peak increases with increasing temperature, the hydrogen bonds between water molecules break, a small portion becomes FW, and most of it evaporates with increasing temperature. Compared to rGO, a peak was observed for rGOFpl-3 at 3064 cm^{-1}, which is thought to be an absorption peak generated by the higher polarity Fpl attracting more FW and forming more IW. Again, the area of this peak increased with increasing temperature, as shown in Fig. S5.† In addition, the FTIR spectra of the dried rGO and rGOFpl-3 foams showed that rGO and rGOFpl-3 have no characteristic absorption peaks at 3200–3650 cm^{-1}, as shown in Fig. S6,† which also indicates that the absorption peaks here are only from the –OH vibrations of water molecules.

The Raman spectra of rGOFpl-5 and rGOFpl-3 were measured after moderate water absorption, and subsequently, four peaks were obtained by fitting with a Gaussian function, respectively. It should be noted that as a comparison, the hydrophilicity of rGO is not high, and no obvious water absorption peak is observed after the same treatment (Fig. S7†). The two lower wavenumbers of the four peaks between 3200 and 3450 cm^{-1} are attributed to FW, which can form four hydrogen bonds: two H atoms form two hydrogen bonds with the O atom of another water molecule, and the O atom of the water molecule has two lone pairs of electrons that can form hydrogen bonds with the H atom of another water molecule. On the other hand, the two higher wavenumbers of the peaks between 3500 and 3650 cm^{-1} are attributed to IW, which is in a weak or non-hydrogen bonded state due to the partial or complete breakage of the intermolecular hydrogen bonds of the water molecules here.[26–28] The integral area ratio in Fig. 2e shows that rGOFpl-3 reaches 0.4, higher than rGOFp-5 at 0.37, and they are both higher than pure water at 0.23 (Fig. S8, Table S5 and Note S3†). The introduction of the highly polarity Fpl nanosheets increases the proportion of IW in the water-bearing foam. Compared with rGO without loaded highly polarity Fpl nanosheets, rGOFpl-3, which has more affinity with water molecules, can be wetted rapidly within 0.6 s in Fig. 2f.

In Fig. 3a, the UV vis absorption of rGO and rGOFpl foam in the full wavelength range is about 95%, which is weighted by the standard solar spectrum 1.5 global (AM 1.5 G), the transmittance is 0%, and the reflectivity is less than 5% (Fig. S9 and S10†). rGO and rGOFpl foams have porous surfaces and vertical channels that increase the light absorption area and sunlight reflectance. The solar water evaporation rates of rGO, rGOFpl-5, rGOFpl-3, rGOFpl-2, and rGOFpl-1 foam under 1 sun irradiation within 6 h were 0.98, 1.44, 1.83, 1.48, and 1.06 kg m^{-2} h^{-1},

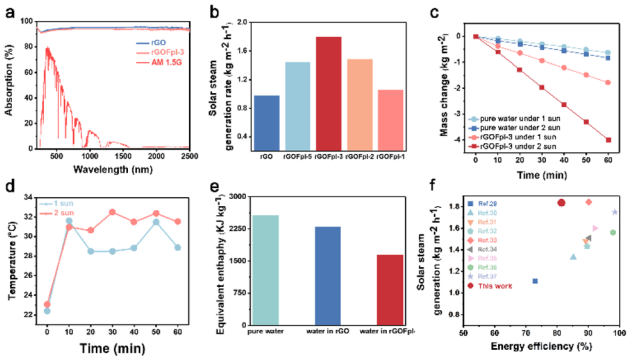

Fig. 3 (a) UV vis NIR spectra of rGO and rGOFpl-3. (b) Solar steam generation rate of rGO and rGOFpl with different ratios under 1 sun irradiation (1 kW m^{-2}). (c) The mass change of pure water and rGOFpl-3 under 1, 2 sun irradiations in 0–60 min. (d) The surface temperatures of the rGOFpl-3 under different solar intensity. (e) The calculated equivalent enthalpy of water in rGO and rGOFpl-3 foam. (f) Comparison of water evaporation performance based on rGO-based solar absorbers.

respectively, of which rGOFpl-3 was the best, as shown in Fig. 3b and S11.† Fpl is a kind of hydrophilic mineral with more electronegative atoms such as O and F, and the polar surface of Fpl tends to make the charge distribution of the O and H atoms of the water molecule redistributed by attracting more hydrogen protons; thus, more IW formed and escaped. See more details in Note S4.†

The water evaporation rate of rGOFpl-3 foam under 1 and 2 sun irradiations were 1.83 and 4.0 kg m^{-2} h^{-1}, respectively, which were 3–5 times of the evaporation rate of pure water, as shown in Fig. 3c. The temperature changes of rGOFpl-3 foam under different sunlight irradiations were subsequently recorded to evaluate its photothermal conversion capacity. Under 1 sun irradiation, the surface temperature of the rGOFpl-3 foam reached 32 °C, as shown in Fig. 3d. The overall rGOFpl-3 foam was filled with water and completely exposed to air; thus, most of the heat generated at the surface of the foam escaped into the air. The surface temperature variations of the dry rGOFpl-3 foam under different sunlight irradiations were also measured, as shown in Fig. S12 and S13.† The highest temperatures of rGOFpl-3 reached 51.6 °C and 84.4 °C under 1 and 2 sun irradiations, respectively, showing the excellent photothermal conversion ability of rGOFpl-3 foam.

The essential reason for the high enthalpy of evaporation of water is the strong hydrogen bonds between water molecules, and the comparison of the enthalpy of evaporation under the same conditions also helps to determine the strength of hydrogen bonding between water molecules. The equivalent evaporation enthalpy of water in darkness was calculated by eqn (1) for rGO and rGOFpl-3 foam as 2287 kJ kg^{-1} and 1632 kJ kg^{-1}, respectively, as shown in Fig. 3e, both of which are significantly lower than the enthalpy of evaporation of pure water of 2560 kJ kg^{-1}. This is further supported by DSC measurements; see Fig. S14† for detail. We suggest that the interfacial charge transfer between the polar surface of the Fpl nanosheets and the adjacent water molecules leads to a weakening of the hydrogen

bonds in the IW, which makes it easier for water molecules to escape from the evaporation interface. The charge transfer effect of the highly polar Fpl nanosheets on the interfacial water molecules allows more IW to be generated in the rGOFpl-3 foam. rGOFpl foam therefore has a high energy conversion efficiency (η). The η of the rGOFpl-3 foam obtained by eqn (2) is 81.4%. Comparing the previous works, the evaporation performance of rGOFpl is found to be better than most typical rGO-based solar absorbers, as summarized in Fig. 3f and Table S6.†[29–37]

FP calculations and MD simulations investigated the kinetic process of microscale evaporation with the aim of demonstrating the effect of charge transfer due to the surface polarity of solar absorbers on the evaporation rate. Based on the observation of three evaporation phases of hydrogels at the macroscopic scale,[38] it is generally believed that IW molecules are more likely to evaporate because it is difficult to form tetrahedral conformations and have weaker intermolecular hydrogen bonds. Fig. 4a and b show unit cell of Fpl nanosheets, where the chemical components having good polarity are exposed on the surface, including KO, MgO, and MgF_2. FP calculation was performed to apply the Bernal–Fowler ice model[39] embedded in the studied substance and to study their influence on the evaporation acceleration, using MgF_2, shown in Fig. 4c as an example. In this way, the variation of the water molecule near the surface of Fpl nanosheets could be studied at the electronic level. The corresponding charge difference distribution of MgF_2@Ice is shown in Fig. 4d, and a significant charge transfer is observed. Quantitative charge changes (with respect to ice) can be obtained by charge analysis (Bader charge analysis) and are marked in Fig. 4c with a charge transfer of 0.1–0.2 e^- between MgF_2 and adjacent BW molecules. Note that when O atoms gain charges, H atoms lose charges, indicating the weaker polarity of the adjacent BW molecules. In fact, not only do MgF_2, K_2O, and MgO have the same phenomena, the charge transfer amplitude also changes a little (see Fig. S15†). The charge transfer weakens the polarity of water molecules, which was investigated by MD simulations. It was found that the evaporation rate increases as the water molecules' polarity decreases and follows the Arrhenius relation,

$$k = A\exp(-Q(p)/k_BT) \quad (3)$$

where k is the evaporation rate, A is the frequency factor equaling to 4.294×107 ns^{-1}, k_B is the Boltzmann constant, T is the temperature, $Q(p)$ is the activation energy and is a linear function of polarity p (defined by the amplitude of the partial charge on O atom), *i.e.*, $Q(p) = (p/p_r)Q_r$, where $p_r = 0.82$ and $Q_r = 1.34$ eV (see Fig. 4e), indicating that the mechanism of evaporation remains unchanged, and the energy barrier height of evaporation is decided by the polarity. Combining the charge transfer and its induced hydrogen bond weakening, our theoretical calculation suggests that charge transfer between adjacent BW molecules and hydrophilic materials is a key step that weakens the hydrogen bond between IW and BW and therefore provides the IW molecules a better chance to escape from the liquid surface. One thing should be stressed that the charge fluctuation amplitude of O atoms in IW could attain 0.02 e^- (circled by black dash lines in Fig. 4c), which could affect the hydrogen bond strength. These bonds determine the evaporation rate, assuming an O atom loses 0.02 e^-; the corresponding polarity is reduced to 0.8, leading a 3.5-folds enhancement in the evaporation rate (according to eqn (3)), which is close to the two times the increase in the evaporation rate of rGOFpl-3 relative to rGO found in experiments (see Fig. 3b).

To give a more specific physical picture for the accelerated evaporation of the IW molecules, in Fig. 4f, two types of water molecules with different polarities are mixed to qualitatively reproduce the evaporation dynamic process, where the strength of the hydrogen bond varies. It is found in the limited simulation time that only water molecules possessing weaker hydrogen bonds manage to run away, resembling the accelerated evaporation of the IW molecules.

An index is proposed to assess the electronegativity difference of different matters (*e.g.*, MgO, MgF_2, and Al_2O_3) in contact with water molecules.

$$e_n = e_A - \sum_{i=1}^{NN} e_i/N_i - e_C \quad (4)$$

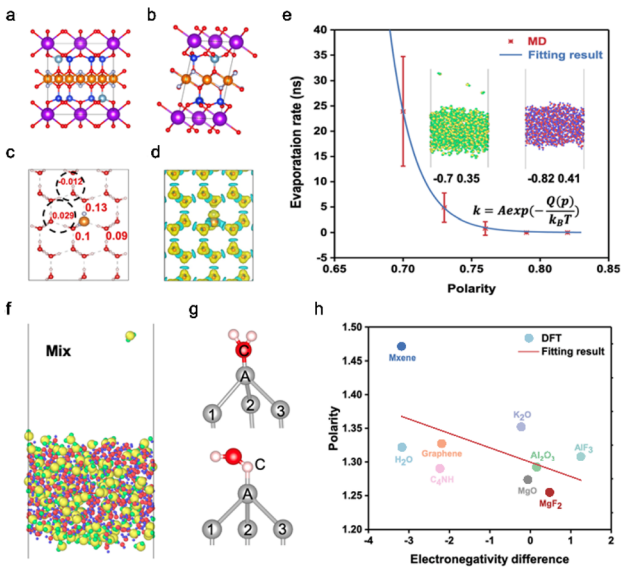

Fig. 4 Correlation between polarity and evaporation rate. (a) and (b) show the front and side view of the unit cell in Fpl ($K\{Mg_3[AlSi_3O_{10}]F_2\}$), respectively. The purple, orange, light blue, blue, red, and grey color, represent K, Mg, Al, Si, O, and F atoms, respectively. (c) Polarity model: one Mg and two F atoms are embedded in Bernal–Fowler ice model, where the charge number variation of the given O atoms are marked. The corresponding charge density difference is given in (d), where yellow (blue) color represents positive (negative) charge accumulation. (e) By gradually tuning the charges on H and O atoms in MD simulation, the polarity dependence of evaporation rate is studied. Note that the polarity is equal to the number of electrons attracted by O atoms. (f) Two kinds of water molecules with different polarities are mixed in MD simulation, only those with weaker polarity could evaporate. (g) The illustration of electronegativity difference index. (h) The polarity as a function of electronegativity difference.

where e_n is the electronegativity difference, e_A, e_i, and e_C are the charge of corresponding atoms (see Fig. 4g, where A and C are marked, and i represents the i-th nearest neighbor atom of A). NN and N_i is the coordination number of A and its i-th nearest neighbor atom, respectively. Note that C could represent O or H atom. The results (see Fig. 4h) show that a strong association between the polarity and the electronegativity differences (polarity is still defined by the amplitude of the partial charge on O atom, and the value difference with Fig. 4e origins from the calculation methods). Therefore, the correlation between them and the evaporation rate can also be helpful in searching the potential candidate for accelerating water evaporation. Compared with other materials commonly used for water evaporation, MgF_2 and MgO, which may appear on the surface of Fpl nanosheets, lead to the minimal polarity for the adjacent BW molecules, which work together to accelerate the water evaporation in our system and make the rGOFpl foam perform better (Fig. 3f and 4h). See Note S5 in the ESI† for more computation details.

The device shown in Fig. 5a and S16† was used for water collection. The rGOFpl foam can work continuously as an absorber for 12 h with stable water evaporation rate, as shown in Fig. 5b. Seawater desalination using rGOFpl foam revealed that a small amount of salt particles accumulated on the foam surface, leading to the blockage of the foam channels. The water evaporation rate of rGOFpl foam then decreased to 1.6 kg m^{-2} h^{-1} after 6 h for 1 sun (see Fig. 5c and inserts in Fig. 5c). The concentrations of the four major ions, including Na^+, K^+, Ca^{2+}, and Mg^{2+} in the condensate and collected water, decreased significantly from the initial 14 700, 669, 377, and 1130 mg L^{-1} to 8.37, 0.709, 2.97, and 0.636 mg L^{-1}, respectively, as shown in Fig. 5d, with all salt rejection efficiencies close to 100%. All these concentrations were well below the drinking water standards set by the World Health Organization (WHO).

The ability of the rGOFpl foam to purify simulated pharmaceutical wastewater was also evaluated using drugs including metronidazole and atenolol with good water solubility (concentration of 1000 mg L^{-1}), ciprofloxacin with good acid solubility, and ibuprofen with good base solubility (concentration of 200 mg L^{-1}). During 6 h of water evaporation, the rGOFpl foam still maintained a water evaporation rate of 1.74 kg m^{-2} h^{-1}, as shown in Fig. 5e. By plotting the standard UV vis absorption curve (Fig. S17†), the residual drug concentration in the condensed and collected water was obtained. As shown in Fig. 5f, the removal efficiencies were as high as 99%, 100%, 99.7%, and 96.1% for metronidazole, atenolol, ciprofloxacin, and ibuprofen at concentrations as low as 9.89, 0.28, 0.55, and 6.56 mg L^{-1}, respectively, and these results were superior to many reported works using adsorption methods for water pollution treatment (Fig. 5g).[40–74] In addition, rGOFpl foam was used to purify the aqueous solution containing the artificial dye Rhodamine B. It was found that the UV vis characteristic peak of Rhodamine B in condensed and collected water at 570 nm disappeared after purification, and the purification efficiency was close to 100% with the color of the solution changing from pink to colorless, as shown in Fig. 5h and i.

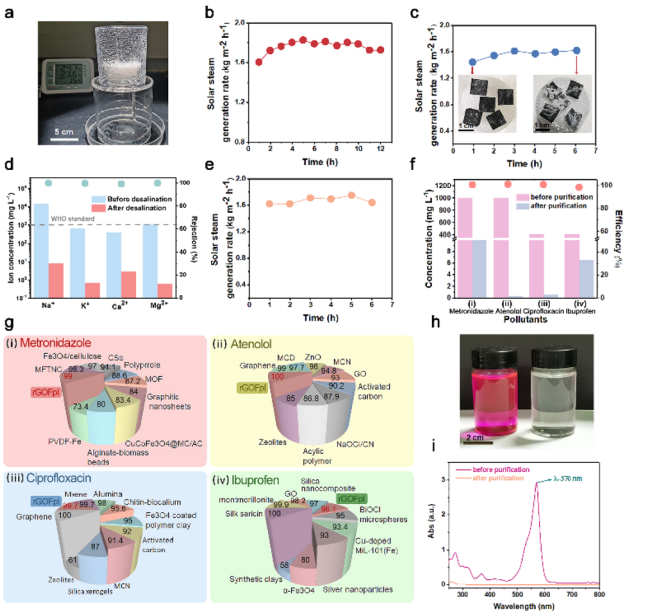

Fig. 5 (a) Photograph of water evaporation and collection system. (b) The evaporation performance of the rGOFpl foam in 12 h under 1 sun. (c) The evaporation performance of the rGOFpl foam with seawater in 6 h under 1 sun; insets are pictures of before and after evaporation with salt accumulation. (d) Concentration measurement of four main ions before and after purification and calculated ion rejection efficiency in seawater (Yellow Sea). (e) Solar steam generation rates of metronidazole in 1000 mg L^{-1} during 6 h under 1 sun. (f) Purification efficiency (collected water) of rGOFpl solar absorber for 4 simulated pharmaceutical wastewaters, (i) metronidazole, (ii) atenolol, (iii) ciprofloxacin, (iv) ibuprofen. (g) Comparison with adsorption method for the treatment of pharmaceutical wastewater. Overall, the rGOFpl solar absorber has the highest purification efficiency. (h) Photos of the rGOFpl solar absorber before and after purification of Rhodamine B solution (100 mg mL^{-1}); it is obtained by continuous exposure to 3 suns for 5 h, and (i) UV vis absorption curves of the solution before and after purification.

Conclusion

In summary, the water evaporation rate of 1.83 kg m^{-2} h^{-1} for rGOFpl foam is sufficient to make it stand out among common rGO-based solar absorbers due to the weakening effect of hydrogen bonds between intermediate water molecules induced by highly polar units. FP calculations and MD simulations explain the mechanism by which the uniformly-dispersed strongly polar Fpl nanosheets on the rGO surface affect the charge distribution of water molecules in the adjacent BW layer, which in turn weakens the intermolecular hydrogen bonds in the intermediate water layer and promotes the rapid evaporation of water. This design is very helpful for scientists to understand the basic principles of rapid evaporation of water in photothermal materials below the boiling point of water at the level of hydrogen bond formation and its nature.

Author contributions

L. W., N. C. and F. L. conceived this project. L. W. synthesized and characterized materials, performed water evaporation and

purification experiments of rGO and rGOFpl foam. L. W., N. C. and F. L. analyzed the experiments data and wrote the paper. L. W., Y. Y., X. L., X. S., Z. W., T. Y., and L. Q. proposed important experimental insights and solutions. J. L. and F. L. performed the MD simulation and FP calculation and L. W., J. L. N. C. and F. L. wrote some relevant part of this paper.

Conflicts of interest

There are no conflicts to declare.

Acknowledgements

This work was supported by NSFC (22279010, 21671020, 51673026, 22035005, and 52073159), Natural Science Foundation of Beijing Municipality (2222075), the National Key R&D Program of China (2017YFB1104300), and Analysis & Testing Center, Beijing Institute of Technology.

References

1 P. Tao, G. Ni and C. Y. Song, *Nat. Energy*, 2018, **3**, 1031.
2 K. Bae, G. Kang and S. K. Cho, *Nat. Commun.*, 2015, **6**, 10103.
3 M. M. Gao, C. K. Peh and H. T. Phan, *Adv. Energy Mater.*, 2018, **8**, 1800711.
4 M. W. Zhu, Y. J. Li and F. J. Chen, *Adv. Energy Mater.*, 2018, **8**, 1701028.
5 M. M. Ye, J. Jia and Z. J. Wu, *Adv. Energy Mater.*, 2017, **7**, 1601811.
6 Y. Zeng, J. F. Yao and B. A. Horri, *Energy Environ. Sci.*, 2011, **4**, 4074.
7 C. J. Chen, Y. J. Li and J. W. Song, *Adv. Mater.*, 2017, **29**, 1701756.
8 Q. S. Jiang, L. M. Tian and K. K. Liu, *Adv. Mater.*, 2016, **28**, 9400.
9 H. Ghasemi, G. Ni and A. M. Marconnet, *Nat. Commun.*, 2014, **5**, 4449.
10 X. Z. Hu, W. C. Xu, L. Zhou, Y. L. Tan, Y. Wang, S. N. Zhu and J. Zhu, *Adv. Mater.*, 2017, **29**, 1604031.
11 X. Liu, Y. Tian and F. Chen, *Adv. Funct. Mater.*, 2021, **31**, 2700977.
12 X. L. Wang, Z. H. Li and Y. Wu, *ACS Appl. Mater. Interfaces*, 2021, **13**, 10902.
13 X. B. Chen, N. L. Yang and Y. L. Wang, *Adv. Mater.*, 2022, **34**, 2107400.
14 Q. C. Lu, W. X. Shi and H. Z. Yang, *Adv. Mater.*, 2020, **32**, 2001544.
15 H. C. Li, H. N. Li and L. Y. Zou, *J. Mater. Chem. A*, 2023, **1**, 2933.
16 R. G. Bryant, M. A. Johnson and P. J. Rossky, *Acc. Chem. Res.*, 2012, **45**, 1.
17 T. Hatakeyema, A. Yamauchi and H. Hatakeyema, *Eur. Polym. J.*, 1984, **20**, 61.
18 T. Terada, Y. Maeda and H. Kitano, *J. Phys. Chem.*, 1993, **97**, 3619.
19 Z. H. Ping, Q. T. Nguyen and S. M. Chen, *Polymer*, 2001, **42**, 8461.
20 T. Wang and S. Gunasekaran, *J. Appl. Polym. Sci.*, 2006, **101**, 3227.
21 K. Kudo, J. Ishida and G. Syuu, *J. Chem. Phys.*, 2014, **140**, 044909.
22 Y. Sekine and T. Ikeda-Fukazawa, *J. Chem. Phys.*, 2009, **130**, 034501.
23 K. Hara, T. Masuike and A. Okabe, *Jpn. J. Appl. Phys.*, 1995, **34**, 5700.
24 K. Hara, T. Masuike and A. Nakamura, *Phys. B*, 1996, **219**, 526.
25 W. S. Hummers and R. E. Offeman, *J. Am. Chem. Soc.*, 1958, **80**, 1339.
26 X. Y. Zhou, Y. H. Guo and F. Zhao, *Adv. Mater.*, 2020, **32**, 2007012.
27 C. X. Li, S. J. Cao and J. Lutzki, *J. Am. Chem. Soc.*, 2022, **144**, 3083.
28 P. P. Zhang, J. Li and L. X. Lv, *ACS Nano*, 2017, **11**, 5087.
29 H. Q. Fan, A. L. Gao and G. F. Zhang, *Chem. Eng. J.*, 2021, **415**, 128798.
30 P. J. Ying, B. Ai and W. Hu, *Nano Energy*, 2021, **89**, 106443.
31 Z. C. Xiong, Y. J. Zhu and D. D. Qin, *ACS Appl. Mater. Interfaces*, 2020, **12**, 32556.
32 C. Chang, M. Liu and L. Li, *J. Mater. Res.*, 2022, **37**, 294.
33 M. T. Jin, Z. T. Wu and F. Y. Guan, *ACS Appl. Mater. Interfaces*, 2022, **14**(10), 12284.
34 F. T. Meng, Y. Zhang and S. F. Zhang, *Ind. Eng. Chem. Res.*, 2022, **61**, 9763.
35 K. F. Yu, P. F. Shao and P. W. Meng, *J. Hazard. Mater.*, 2020, **392**, 122350.
36 J. K. Xiao, J. Z. Gong and M. Dai, *J. Alloys Compd.*, 2023, **930**, 167404.
37 X. F. Deng, Y. Y. Ge and Y. He, *J. Hazard. Mater.*, 2022, **424**, 127433.
38 F. Zhao, Y. H. Guo and X. Y. Zhou, *Nat. Rev. Mater.*, 2020, **5**, 388.
39 J. D. Bernal and R. H. Fowler, *J. Chem. Phys.*, 1933, **1**, 515.
40 A. Amir, *Polym. Sci., Ser. B*, 2020, **62**, 572.
41 X. Wang, Y. Du and J. Ma, *Appl. Surf. Sci.*, 2016, **390**, 50.
42 N. Aarab, M. Laabd and H. Eljazouli, *Int. J. Ind. Chem.*, 2019, **10**, 269.
43 T. Kalhorizadeh, B. Dahrazma and R. Zarghami, *New J. Chem.*, 2022, **46**, 9440.
44 Z. Bonyadi, F. Noghani and A. Dehghan, *Colloids Surf. A*, 2021, **611**, 125791.
45 A. Nasiri, S. Rajabi and M. Hashemi, *Sep. Purif. Technol.*, 2022, **296**, 121366.
46 S. Girijan, M. Kumar and S. Gomber, *J. Environ. Chem. Eng.*, 2021, **9**, 106102.
47 J. Yang, M. Zhu and X. Wang, *J. Taiwan Inst. Chem. Eng.*, 2015, **49**, 113.
48 A. M. E. Khalil, F. A. Memon and T. A. Tabish, *Chem. Eng. J.*, 2020, **398**, 125440.
49 M. Son, K. Jeong and N. Yoon, *Chemosphere*, 2021, **276**, 130133.
50 P. Bhattacharya, D. Mukherjee and N. Deb, *J. Environ. Chem. Eng.*, 2020, **8**, 103803.

51 M. M. Amin, B. Dehdashti and L. Rafati, *Desalin. Water Treat.*, 2018, **133**, 212.
52 G. Z. Kyzas, A. Koltsakidou and S. G. Nanaki, *Sci. Total Environ.*, 2015, **537**, 411.
53 N. K. Haro, P. Del Vecchio and N. R. Marcilio, *J. Cleaner Prod.*, 2017, **154**, 214.
54 B. Dehdashti, M. M. Amin and A. Gholizadeh, *J. Environ. Health Sci. Eng.*, 2019, **17**, 281.
55 Y. C. Tang, Z. Q. Chen and Q. X. Wen, *Chem. Eng. J.*, 2022, **446**, 137175.
56 E. Sarti, T. Chenet and C. Stevanin, *Molecules*, 2020, **25**, 3331.
57 A. A. Ghani, A. Shahzad and M. Moztahida, *Chem. Eng. J.*, 2021, **421**, 127780.
58 T. H. Dao, N. T. Nguyen and M. N. Nguyen, *Polymers*, 2020, **12**, 1554.
59 R. Zhao, Y. X. Wang and Y. Y. An, *J. Hazard. Mater.*, 2022, **423**, 126917.
60 V. Arya and L. Philip, *Microporous Mesoporous Mater.*, 2016, **232**, 273.
61 A. Avcı, İ. İnci and N. A. Baylan, *Water, Air, Soil Pollut.*, 2019, **230**, 250.
62 A. Avcı, İ. İnci and N. Baylan, *J. Mol. Struct.*, 2020, **1206**, 127711.
63 G. Guzel Kaya, E. Aznar and H. Deveci, *Sustainable Chem. Pharm.*, 2021, **22**, 100483.
64 D. Zide, O. Fatoki and O. Oputu, *Microporous Mesoporous Mater.*, 2018, **255**, 226.
65 V. K. Verma and S. Subbiah, *Ind. Eng. Chem. Res.*, 2017, **56**, 10142.
66 J. Martín, M. d. M. Orta and S. Medina-Carrasco, *Appl. Clay Sci.*, 2019, **171**, 29.
67 P. Banerjee, P. Das, A. Zaman and P. Das, *Process Saf. Environ. Prot.*, 2016, **101**, 45.
68 S. Chandrashekar-Kollarahithlu and R. M. Balakrishnan, *J. Cleaner Prod.*, 2021, **294**, 126155.
69 J. Li, S. Y. Sun and R. Chen, *Environ. Sci. Pollut. Res.*, 2017, **24**, 9556.
70 P. Xiong, H. Zhang and G. L. Li, *Sci. Total Environ.*, 2021, **797**, 149179.
71 Y. Vicente-Martinez, M. Caravaca and A. Soto-Meca, *Sci. Rep.*, 2020, **10**, 18288.
72 M. Ulfa, D. Prasetyoko and H. Bahruji, *Materials*, 2021, **14**, 6779.
73 R. Devesa-Rey, J. del Val and J. Feijoo, *Water*, 2021, **13**, 2394.
74 Z. Zabihi and M. Homayoonfal, *Polym. Adv. Technol.*, 2021, **32**, 4765.